Tribological origin of squeal noise in lubricated elastomer–glass contact

F. Dalzin [a,b], A. Le Bot [a], J. Perret-Liaudet [a], D. Mazuyer [a,*]

[a] *LTDS-UMR 5513 CNRS, Ecole Centrale de Lyon, 36, Avenue Guy de Collongue, 69134 Ecully Cedex, France*
[b] *Valeo 1 Avenue Pierre et Marie Curie, 63500 Issoire, France*

A B S T R A C T

An experiment of squeal noise on a lubricated elastomer/glass contact is presented. The experimental device, stiff enough to be non-intrusive on the system response up to several kHz, provides the contact force, vibration velocity and contact image with a high sampling rate. It is shown that the self-excited oscillation responsible of squeal involves a single mode and that its apparition is induced by the velocity weakening of friction. Direct observation of the contact by microscopy highlights that the contact is highly heterogeneous and the number of contact spots decreases with the sliding velocity during squeal.

© 2016 Elsevier Ltd. All rights reserved.

1. Introduction

Noise annoyance caused by friction-induced vibration is a major issue encountered in a lot of mechanical systems. To cite a few, typical engineering examples are vehicle brakes [1–7], friction clutches [8], train wheel–rail in curves [9–11], waist seal rubber sliding on glass [12], wiper blade systems [13–16], frictional belts [17] and machine tools [18]. The resulting noises are generally referenced as chatter [19], squeak [20], and squeal [21,22]. All these sounds are produced by a combination of forcing or self-excited nonlinear oscillations of the mechanical system in the presence of a friction force [23–26]. The existence of a coupling between the friction force and the resulting motion induces a loss of stability of the equilibrium state which leads to self-excited oscillations.

Sprag-slip is a typical example of this kind of instability. A coupling between the normal load and the friction force is enforced by a geometrical effect. The normal force and therefore the friction force depend on the solid position. A second example is the mode coupling instability. To describe this phenomenon, a multi-degree of freedom model is required [27,28]. By introducing the normal contact stiffness, a normal vibration at the contact is allowed and again the friction force depends on the solid position. In these two examples, friction is necessarily present but is not constrained to follow a given law. In particular, these instabilities may occur with a friction coefficient independent of the sliding velocity.

This is not the case for the stick-slip vibration phenomenon [29,30]. Stick-slip can simply be explained on the basis of a single-degree-of-freedom system with a frictional sliding mass presenting a kinetic friction weaker than the static friction. This model describes the vibration by a sawtooth displacement–time history where slip and stick phases alternate. An accurate description of the phenomenon generally requires more refined models for friction [31,32]. Some of them include

---

* Corresponding author.
E-mail addresses: fabien.dalzin@ec-lyon.fr (F. Dalzin), alain.le-bot@ec-lyon.fr (A. Le Bot), joel.perret-liaudet@ec-lyon.fr (J. Perret-Liaudet), denis.mazuyer@ec-lyon.fr (D. Mazuyer).

stiction, hysteresis and acceleration effects [33,34]. One can cite for example the rate-and-state friction law, originally developed to simulate seismic cycles [35–37], and the LuGre model originally developed by the automation community [38]. Stick-slip instability is always induced by the weakening of the friction force with the sliding velocity [39]. This velocity weakening leads to an effective negative damping which results in a Hopf bifurcation [40]. In this scenario, the coupling of friction force with motion occurs by the friction–velocity law.

In this general framework, a scientific challenge is to better understand friction instabilities in terms of the tribological behaviour of interfaces. This paper addresses this particular question.

Tribology is particularly important for wet and/or lubricated contacts [41–46]. The friction force and the sliding velocity are linked by the formation of a fluid interface. The degree of separation of the surfaces determines the lubrication regimes: boundary, mixed, elasto-hydrodynamic and hydrodynamic one. The Stribeck effect [47] governs the transition between the boundary and hydrodynamic regimes.

To investigate the origin of the squeal noise of a lubricated contact, this study presents the results of an experiment conducted on an elastomer sample sliding on a glass surface in the presence of water. The experimental device is designed to be much stiffer than the sample. Therefore, the vibration is confined to the sample alone. By observing the contact by microscopy through the glass, we shall investigate the link that exists between the produced noise and the tribological behaviour of the interface at the microscopic scale.

The paper is organized as follows. Section 2 describes the tribometer, the optical viewing system, and the elastomer sample. Section 3 presents the experimental results. The characteristics of squeal noise are analysed and the modal analysis of the sample is performed. Measurements of the squeal noise level and velocity weakening friction are also presented. Section 4 is a discussion on the role of the evolution of contact area during the squeal. Finally, some conclusions are drawn in Section 5.

2. Description of the experiment

2.1. Experimental set-up

The principle of the experiment is shown in Fig. 1. It consists of observing the contact during the occurrence of squeal. An elastomer sample is pressed against a glass disk with a fixed normal load. The contact is lubricated by water. The disk rotation speed is maintained constant during recording of the noise.

The radius of the disk is 45 mm and the mean distance between the sample and the centre of the disk is 22.5 mm. For all the experiments reported in this paper, the contact is lubricated by 10 ml of distilled water introduced by a pipette near the contact zone. The contact is observed through the glass disk with an optical microscope and a white light source at normal incidence.

The driving velocity ranges from 0.8 to 2100 mm s^{-1} and is accurately imposed by a brushless synchronous motor. The speed is regulated by a high resolution encoder allowing 400 000 tic per revolution which measures the instantaneous speed at 1 kHz. The speed accuracy is better than 1 percent for all speeds.

The static normal force is applied by a micrometer screw in the range 0–100 N. It is controlled with a strain gauge of resolution 0.01 N. The tangential force is measured with a piezoelectric sensor with a high frequency bandwidth.

A laser vibrometer Polytech OFV-505 measures the vibration at one point located on the centre of a sample side. The same signal is processed by two decoders in the controller. The first decoder DD500 delivers the displacement with a resolution of 15 pm. The second decoder VD06 operates by Doppler effect and delivers the vibrational velocity with a resolution of 0.05 µm s^{-1}. The signals corresponding to the normal force, tangential force, vibrational velocity and vibrational displacement are acquired synchronously by an analogue-to-digital data acquisition card at the sampling frequency 20 kHz.
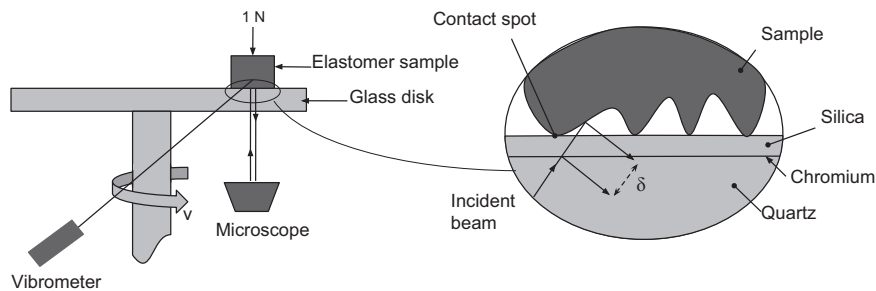

Fig. 1. Principle of the experiment. (For interpretation of the references to color in this figure caption, the reader is referred to the web version of this paper.)
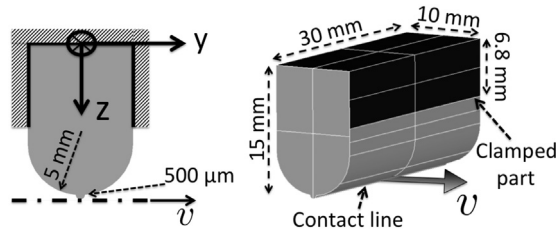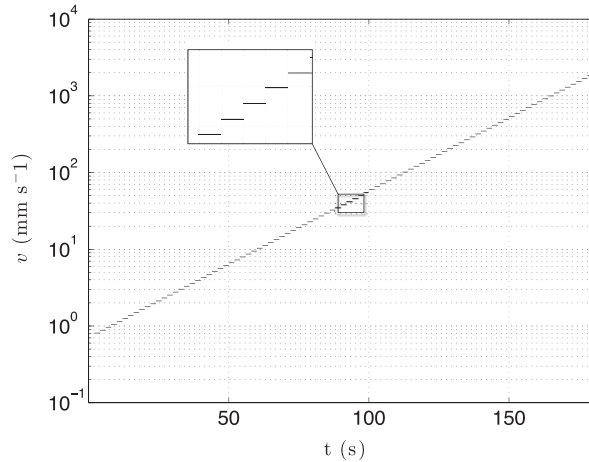
Fig. 2. Elastomer sample.

Fig. 3. Driving velocity time evolution.

2.2. Optical viewing system

In order to perform interferometric image of the contact, the glass disk is made of quartz and is coated with a chromium layer which is itself covered by a silica layer of thickness 10 nm (Fig. 1). The sample is therefore in contact with silica. The incident light beam is divided into two beams, one is reflected by the chromium layer, and the other one goes through the silica layer and the interface before being reflected by the elastomer surface. The difference of optical path between the two beams generates an interferometric image where the pixel colour depends on the distance between the chromium layer and the elastomer.

A camera with a resolution of 2448×2050 pixels is equipped with a varying zoom allowing a full size image from 7 mm × 5.9 mm to 0.95 mm × 0.8 mm. It records video at the rate of 9 frames per second.

2.3. Elastomer sample

The elastomer sample is an extruded profile of 30 mm length, as shown in Fig. 2. The profile consists of a half disk of 10 mm diameter extended by a 10 mm right section. It has overall dimensions of 15 mm height and 10 mm width. Furthermore, a small cylinder of radius 0.5 mm is placed at the bottom of the main cylinder. The contact with the glass is achieved along a generating line of this small cylinder (x-axis).

The sample is clamped in a rigid sample holder at its top side and along two vertical sides of height 6.8 mm. The glass disk is in contact with the sample bottom. The driving velocity is perpendicular to the contact line in the y-axis direction.

The roughness of the elastomer surface is $R_a = 500$ nm. This value has been measured with a Bruker Contour GT-K1 optical microscope with a $50\times$ lens. The glass disk is polished and has a roughness estimated at few nm. The sample is made of a raw synthetic elastomer and has the following mechanical properties. Young's modulus is obtained experimentally by dynamic mechanical analysis measurement (see Appendix A). The sample has been excited in the frequency range 0.1–30 Hz and temperatures from $-30\,°C$ to $+23\,°C$ with a magnitude of 1 μm. The master curve gives Young's modulus $E = 8.91$ MPa at 23 °C and 2 kHz. The density is measured by weighing the sample with a precision balance and measuring its volume by immersing it in a beaker containing water. We have obtained $\rho = 1400$ kg m^{-3}. Poisson's ratio of elastomers is estimated from the literature as $\nu = 0.5$.
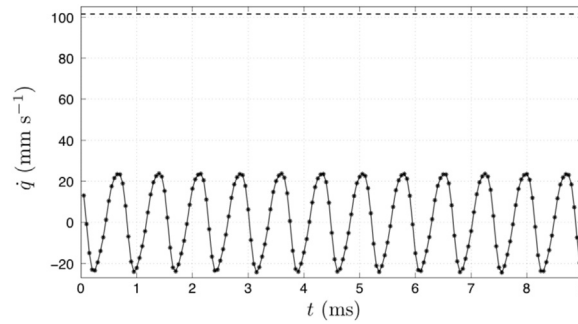
Fig. 4. Time-history of vibration velocity at $v = 101.5$ mm s^{-1}: vibration velocity (solid line) and driving velocity (dashed line).
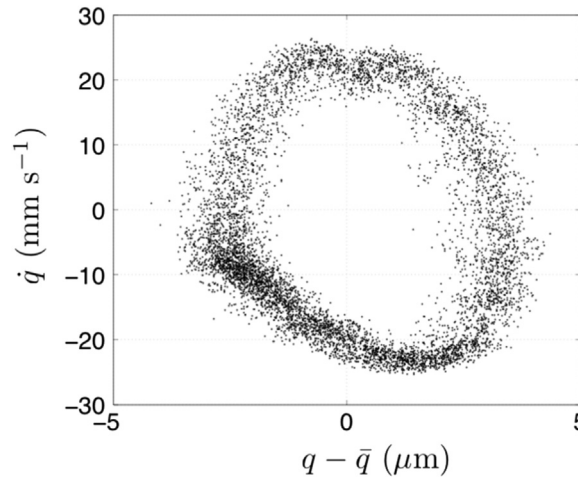

Fig. 5. Phase space of the vibration at $v = 101.5$ mm s^{-1}.

2.4. Measurement protocol

Before all tests, the glass disk is cleaned in an ultrasonic bath of isopropanol. The elastomer sample is pressed on the disk with a normal load of 30 N m^{-1}, the disk being at rest. A photograph of the dry contact without water is taken. Then, 10 ml of distilled water is placed on the glass disk. Another photograph of the contact with water is taken. The disk is rotated for 2 min at the driving velocity $V = 800$ μm s^{-1} to stabilize the contact. Then, the measurement phase starts. The driving velocity increases in a logarithmic progression from 800 μm s^{-1} to 2.2 m s^{-1} in 101 steps. For each step, the driving velocity is maintained constant during 2 s, as shown in Fig. 3.

A video film of the contact evolution is recorded simultaneously with other signals. At the end of the experiment, the disk is stopped and the sample is lifted. This experiment is repeated with four different samples of the same elastomer, at an ambient temperature of ≈ 22 °C.

3. Experiment results

3.1. Squeal noise analysis

Fig. 4 shows the time evolution of the y-component of the vibrational velocity $\dot{q}$ at the measurement point delivered by the vibrometer. As can be seen, the oscillation is almost a pure sine wave. The peak-to-peak amplitude is equal to 46 mm s^{-1} which is below the driving speed of the glass disk $v = 101.5$ mm s^{-1}.

The vibrometer also delivers the y-component of the vibrational displacement q. The phase portrait shown in Fig. 5 is plotted from the signals displacement q and velocity $\dot{q}$ synchronously acquired. The constant displacement component (static deflection) has been subtracted. The trajectory is a limit cycle close to an ellipse centred at the origin. Remind that for classical stick-slip instability, the vibration velocity is equal to the driving velocity during the stick phases. This induces a flattening of the upper part of the ellipse in the phase portrait [30,48,49]. However, it appears from Figs. 4 and 5 that the vibration velocity never reaches the sliding velocity and that the ellipse is not flattened. This shows that there is no stick
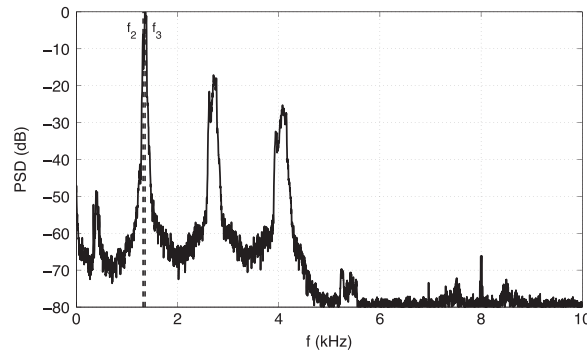
Fig. 6. Power spectral density (PSD) of the vibration velocity signal (solid line); Modes 2 and 3 natural frequency (dashed line).
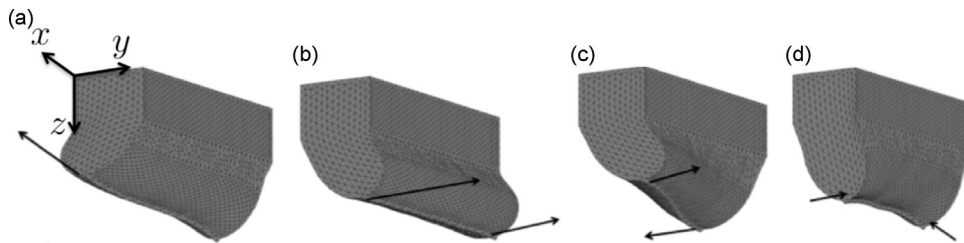

Fig. 7. First modes of the elastomer sample: (a) Mode 1, $f=1152$ Hz; (b) Mode 2, $f=1320$ Hz; (c) Mode 3, $f=1359$ Hz; (d) Mode 4, $f=1551$ Hz.

phase during the vibration. Furthermore, the analysis of images shows that there is no deformation of the interface which moves as a rigid body. Up the scale of micrometre which is the microscope resolution, no spot reaches the driving velocity and there is therefore no local sticking.

The power spectral density (PSD) of the vibration velocity response is shown in Fig. 6. The PSD has been calculated with a Hanning filter with 8192 lines and an overlap of 20 percent. It reveals the purely harmonic nature of the vibration with a fundamental frequency $f_0 = 1387$ Hz and its second and third harmonics with respective levels of 19 and 27 dB below, respectively.

3.2. Modal analysis

After this brief description of the squeal noise, it is of interest to determine which modes may be involved in the vibration. To this end, a modal analysis has been performed to determine the first mode shapes of the sample and their natural frequencies by using the finite element method. However, this numerical model does not aim to predict the apparition of the instability.

The geometry of the sample is discretized with 4-node-tetrahedral isoparametric elements with a total number of degrees of freedom ranging from 15 000 to 300 000. These numbers of dof are large enough to ensure a good accuracy of the results on the first modes. The computation has been conducted with two different softwares, Catia and Aster. A linear elastic behaviour has been assumed in elements. Material properties are density 1400 kg/m³, Young's modulus 8.91 MPa and Poisson's ratio 0.49. These values are obtained by a direct measurement and not by updating. In particular the Young modulus value is taken from measurements at a frequency (2 kHz) close to the expected eigenfrequencies. Constraints with null displacement are imposed to model the attachment at the sample holder. Free boundary conditions are imposed elsewhere including the sliding contact line. The absence of stick phase in measured signals leads to a friction force which is only velocity-dependent. The contribution of an elastic component of the friction force is negligible in this case.

The first four eigenmodes and their natural frequencies are shown in Fig. 7. Mode 1 corresponds to a longitudinal deformation of the base along the contact line (x-axis). This deformation being normal to the sliding velocity, this mode cannot be excited. Mode 2 is a deformation of the sample along the y-axis. As the sliding velocity is also oriented in the y-axis, this mode can of course be excited by the friction force. Mode 3 corresponds to a twist deformation around the vertical z-axis. A friction force oriented in the y-direction and uniform along the contact line cannot excite this mode. However, due to the circular movement, the sliding velocity is slightly lower near the centre of the disk than the outer extremity of the sample. Furthermore, elastomer is a highly damped material, it is therefore not excluded that modes 2 and 3 may be coupled by damping. A last reason for the apparition of mode 3 could be heterogeneity of the contact conditions along the contact line. Mode 4 presents deformations within the x, z-plane which is normal the disk plane. The very low roughness of the disk cannot generate this kind of out-of-plane motion.

The PSD of the vibration velocity response is shown in Fig. 6 with a frequency resolution of 2 Hz. Vertical dashed line indicates the position of the second and third eigenfrequencies. The PSD presents a single maximum close to the second or
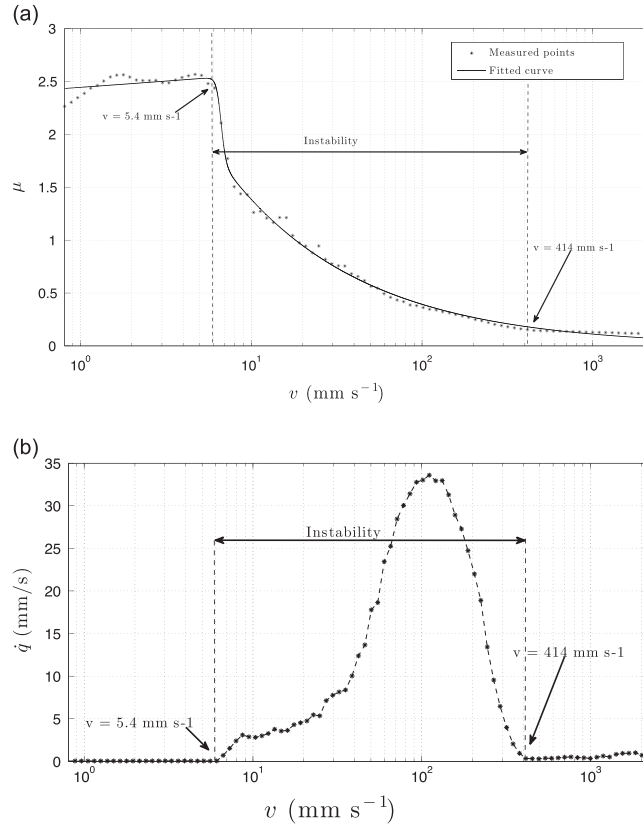
Fig. 8. Evolution of friction coefficient and vibrational velocity with sliding velocity: (a) μ versus v; (b) amplitude of the vibration velocity versus v.

third eigenfrequency. The difference between these two eigenfrequencies being $\Delta f = 39$ Hz, the modal damping ratio ζ must be lower than $\Delta f / 2f \approx 1.5$ percent in order to distinguish them. This value lower than usual damping ratio values for an elastomer.

The frequency resolution is 2 Hz and the half-power bandwidth is of order of 80 Hz. It does not permit the differentiation between modes 2 and 3, but with the camera especially adjusted to visualize a large area of contact, we observed that all points of the contact vibrate in phase. We therefore exclude the presence of mode 3 in the vibration.

In summary, one can consider that only one mode is involved in the vibration. As a consequence, the only origin of the instability is the velocity weakening effect of friction.

3.3. Velocity weakening friction

This section investigates the occurrence of instability and the evolution of the friction coefficient for increasing sliding speeds.

Fig. 8(a) shows a Stribeck type evolution of the friction coefficient μ versus the sliding velocity v. At low sliding velocities ($v < 5.4$ mm s^{-1}), μ is high (≈ 2.5) which corresponds to the value of dry friction between elastomer and glass. For intermediate sliding velocities (5.4 mm s$^{-1} < v < 1$ m s^{-1}), there is a velocity weakening dependence of μ. For higher velocities ($v > 1$ m s^{-1}) the friction coefficient μ is maintained at a low value due to the formation of a hydrodynamic water layer.

The friction coefficient $\mu = f(v)$ versus the sliding velocity v fits the following function proposed by Bongaerts et al. [50]

$$f(v) = c(v\eta)^q + \frac{1}{1 + (\frac{v\eta}{b})^p}\left[a(v\eta)^n - c(v\eta)^q\right] \tag{1}$$

where $\eta = 1.002$ mPa s is the viscosity of water. This expression contains six parameters. The value of b fixes the transition between high and low values of the friction coefficient μ. The slope during the transition is governed by the exponent p. In addition, a and n give the behaviour at low velocities while c and q drive the asymptotic behaviour at high speeds.

From Fig. 8(a), the coefficients have been identified by the least mean square algorithm. They are $a = 2.26 \times 10^{-3}$(Pa m)$^{-n}$, $b = 6.63 \times 10^{-6}$ Pa m, $c = 2.5408$ Pa m,$^{-q}$, $p = -32.972$, $q = 0$ and $n = -0.5467$. The interpolated function f is plotted as a solid line in Fig. 8(a).
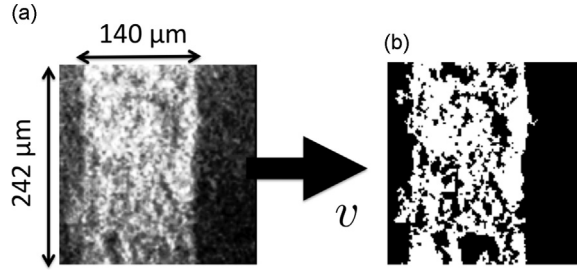
Fig. 9. Example of elastomer–glass contact with sliding velocity vector v: (a) original photography of contact; (b) contact spots (white pixels).

Fig. 8 (b) shows the evolution of the amplitude of the vibration velocity versus the sliding speed. For increasing sliding speeds, the vibration appears at $v = 5.4$ mm s^{-1} and disappears beyond $v = 414$ mm s^{-1}. We have also performed this experiment for decreasing speeds and observed that the speed range of the instability remains the same. The maximum vibration is reached at $v = 110$ mm s^{-1} with an amplitude of 33.6 mm s^{-1}.

Comparison of Fig. 8(a) and (b) highlights that the instability only occurs for intermediate sliding velocities for which the friction coefficient μ strongly decreases. Furthermore, the vibration velocity always remains lower than the sliding velocity and this confirms that a stick phase has not been observed.

4. Discussion

4.1. Instability range

The conveyor–belt model with a single degree of freedom as studied for instance by Le Rouzic et al. [51,16,52] is sufficient to describe the system behaviour. In this model, the stability is governed by the velocity dependence of the friction coefficient μ. A local stability analysis conducted by linearizing about the fixed point shows that [25] the loss of stability can only occur by a Hopf bifurcation. This bifurcation is driven by the negative derivative slope of μ with respect to the sliding velocity (see Appendix B). Fig. 8 shows that the instability range matches the strongest negative slopes of the friction coefficient in agreement with the model. From Eq. (1), the slope $\mathrm{d}\mu/\mathrm{d}v$ is calculated from the numerical values of the parameters previously identified. An estimation of the slope at $v = 5.4$ mm s^{-1} gives -4.7 s m$^{-1} < \mathrm{d}\mu/\mathrm{d}v < -1 \times 10^{-1}$ s m^{-1} and -3×10^{-1} s m$^{-1} < \mathrm{d}\mu/\mathrm{d}v < -1.6 \times 10^{-1}$ s m^{-1} at 414 mm s^{-1}. In regard to the range -6 s m$^{-1} < \mathrm{d}\mu/\mathrm{d}v < 6.2 \times 10^{-2}$ s m^{-1} for the whole velocity range, these two values may be considered as close. Therefore, one observes that the level of $\mathrm{d}\mu/\mathrm{d}v$ is the same for the apparition and disappearance of the instability. It is known from the conveyor–belt analysis that the sample is unstable within the range $\mathrm{d}\mu/\mathrm{d}v < -C$ where $C = 2\xi k/\omega N$, ξ being the equivalent viscous damping ratio whose main source is the internal damping of the elastomer, k the stiffness at the contact line in the sliding direction, ω the natural frequency of the mode and N the normal load. In the present experiment, an estimation of C gives $C = 2.4 \times 10^{-1}$ s m^{-1}.

One of the keys to the problem is therefore to know the tribological origin of the evolution of the friction coefficient μ versus the sliding velocity v. This is the scope of Section 4.2.

4.2. Analysis of contact spots

The size of the observed area of the elastomer–glass contact has size 1.79 mm $\times$ 1.5 mm. The size of one pixel is 750 nm $\times$ 600 nm. A zoom of a contact image in lubricated condition is shown in Fig. 9(a). Dark zones, mainly localized on the left and right sides of the image, are localized outside the contact zone. The bright zone of width $D_{\mathrm{meas}} = 140$ µm corresponds to the apparent rectangular contact area induced by the 1 mm diameter cylinder of the elastomer sample pressed on the glass disk. According to the Hertzian theory of non-adhesive elastic contact, the theoretical contact width D_{theo} is defined as,

$$D_{\mathrm{theo}} = 2\sqrt{\frac{4FR^*}{\pi l E^*}} \tag{2}$$

where $F = 1$ N is the normal load, $R^* = 0.5$ mm the reduced radius of curvature, $l = 30$ mm the contact length and E^* the reduced Young's modulus at 23 °C and 1 Hz defined as

$$\frac{1}{E^*} = \left[\frac{1 - \nu_{\mathrm{elast}}^2}{E_{\mathrm{elast}}} + \frac{1 - \nu_{\mathrm{glass}}^2}{E_{\mathrm{glass}}} \right] \tag{3}$$

with $\nu_{\mathrm{elast}} = 0.5$, $\nu_{\mathrm{glass}} = 0.2$, $E_{\mathrm{elast}} = 9.3$ MPa, $E_{\mathrm{glass}} = 69$ GPa. Numerical application gives $D_{\mathrm{theo}} = 97$ µm. The theoretical width is inferior to the measured one, indicating that adhesive effects may occur during the elastomer–glass friction in lubricated condition. The contact is heterogeneous and composed of spots. A spot is defined as a set of contiguous pixels
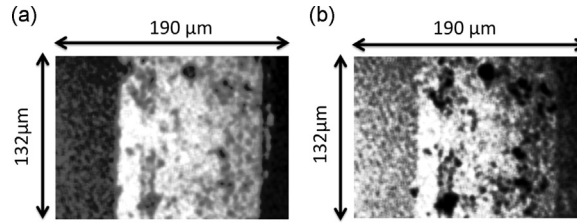
Fig. 10. Experimental identification of contact spots colour: (a) static contact without water; (b) static contact with water.
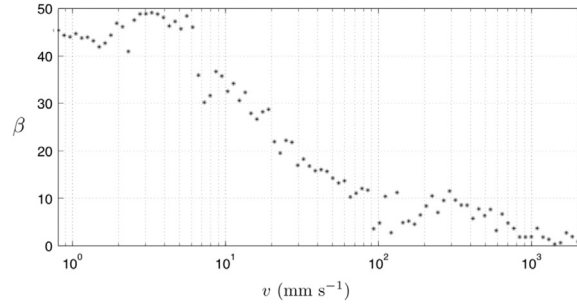

Fig. 11. Area ratio β versus sliding velocity v.

having the same colour. The colour of each spot is related to the optical path δ as shown in Fig. 1. One may define two kinds of spots. The 'contact spots' colour corresponds to where the optical path δ reaches its minimal value. Indeed the optical path is minimal when the distance between the sample and the disk is minimal. The other spots are called 'non-contact spots'. These spots can have different colours corresponding to various separation distances between the elastomer and glass. Thus, there is only one colour defining the contact spots and several colours for the non-contact spots.

In order to identify the contact spots, a first experiment is performed. A static contact (zero sliding velocity) with a constant normal load of 1 N is maintained without water. A first photograph of the contact area is taken and shown in Fig. 10 (a). Then, water is introduced in the contact zone. After 20 s, water completely invaded the contact zone. A second photograph of the contact area with water is taken and shown in Fig. 10(b). In the contact zone, the colour of some pixels does not change after water has been introduced. These pixels are yellow and belong to spots for which the difference of optical path remains unchanged with and without water. The optical path δ is proportional to the refraction index. The refraction index of air is 1 while the refraction index of water is 1.33. Therefore, the only explanation for this colour constancy is that these pixels belong to spots which are directly in contact with glass before and after water has been introduced. This gives the colour of contact spots.

Once the colour of the dry contact spots is defined, an image processing algorithm is used to extract them. This extraction allows the calculation of the area ratio defined in Section 4.3. The camera provides raw images in the RGB colour space. It is converted to HSV colour space where the hue value indicates the pure colour tone. The contact pixels are selected from this value only. Finally, a Gaussian low-pass filter is applied to the resulting binary image to remove noise. An example is shown in Fig. 9(b) where contact spots are represented by white pixels.

4.3. Evolution of surface bearing area

Knowing the contact spots, one can evaluate (within the pixel resolution) the surface bearing area ratio β as,

$$\beta = \frac{A_r}{A_a} = \frac{N_C}{N_T} \tag{4}$$

where A_r is the real contact area, A_a is the apparent contact area, N_C is the number of contact pixels and N_T the total number of pixels in the apparent contact area. The area ratio is then calculated for different sliding velocities v.

Fig. 11 shows the evolution of the area ratio versus the sliding velocity v. Figs. 11 and 8 are obtained from the same experiment and are therefore directly comparable. It is clear that the evolution of the area ratio is somewhat similar to one of the friction coefficients shown in Fig. 8(a). At low sliding velocities ($v < 5.4$ mm s^{-1}), the area ratio is stable around 45 percent. During the intermediate sliding velocities (5.4 mm s$^{-1} < v < 414$ mm s^{-1}), the area ratio decreases until it reaches 8 percent. When $v > 414$ mm s^{-1}, the bearing rate is between 8 percent and 0.2 percent for higher sliding velocities. Examples of contact images in the three regimes are represented in Fig. 12. This decreasing of area ratio with an increasing of sliding velocity has also been observed by Deleau et al. [44] and Wu-Bavouzet et al. [43].
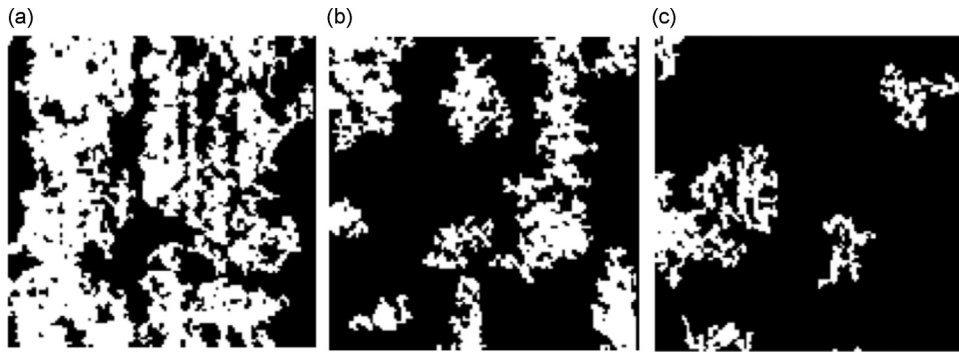
Fig. 12. Contact image in the three regimes: (a) low sliding velocity $v=1$ mm s^{-1} and $\beta=45$ percent. (b) Intermediate sliding velocity $v=11.5$ mm s^{-1} and $\beta=34$ percent. (c) High sliding velocity $v=701.6$ mm s^{-1} and $\beta=7$ percent.
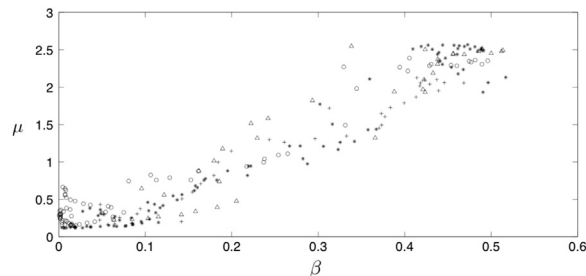

Fig. 13. Evolution of μ versus β for four samples: sample 1 (∗), sample 2 (○), sample 3 (+), and sample 4 (△).

In order to verify the correlation between μ and β, the previous experiment is reproduced four times with different samples of the same elastomer. For each test, the functions $\mu(v)$ and $\beta(v)$ are combined into a single function $\mu(\beta)$. Fig. 13 shows all measurements in the μ, β-plane for the four samples.

The correlation coefficient between μ and β is equal to $r=0.96$. This strong correlation highlights that any change in friction regime is actually due to a change of regime in the contact area. Therefore, to understand the velocity weakening phenomenon at the origin of squeal noise, it appears necessary to analyse the behaviour and the evolution of the contact spots population.

5. Conclusion

In the present paper, an experimental study of the squeal noise of a water-lubricated elastomer–glass contact has been reported. The noise results from friction-induced self-excited vibration which appears to be a pure harmonic cycle, without stick phase. The vibration displacement response mainly involves the second eigenmode of the free-clamped elastomer sample. Bifurcations leading to the unstable sliding state are of Hopf type. The experimental results confirm the role of the negative slope of the friction coefficient versus the sliding velocity. One of the main goals of this study was to correlate the friction coefficient behaviour to the bearing rate. To this end, direct measurement of contact spots population has been performed by using an optical viewing system and by developing a suitable image processing algorithm. One can conclude that the explanation of the appearance of instability by a velocity weakening effect of friction can be interpreted in terms of a rapid detachment of the contact spots implying local contact loss during the mixed regime.

Acknowledgements

Appendix A

The DMA (Dynamic Measurements Analysis) tests are commonly used to measure the viscoelastic properties of materials. The storage modulus E' and the loss modulus E'' can be determined for a given frequency or a given temperature. The

DMA apparatus that has been used in this work is a DMA50 machine manufactured by the company METRAVIB. It works in the temperature range from $-150\,°C$ to $600\,°C$ and in the frequency range from 10–5 Hz to 200 Hz.

In this paper, tensile/compression tests have been performed with a given displacement amplitude of 1 μm, within the following conditions:

- Heating rate: $2\,°C/min$
- Cooling rate: $-2\,°C/min$
- Frequencies: [0.1 Hz; 0.3 Hz; 1 Hz; 3 Hz; 10 Hz; 30 Hz]
- Temperature range: $[-30\,°C; +23\,°C]$

A rubber sample of known dimensions as shown in Fig. A1 is mounted on the DMA apparatus. The sample is stretched with an oscillating displacement $d = d_0 \exp(i\omega t)$ where d_0 and ω are imposed. The resulting force $F_r = F_0 \exp[i(\omega t + \delta)]$ is measured.

There is a phase shift δ between the imposed displacement and the resulting force (see Fig. A2). This allows us to obtain the loss angle $\tan \delta$.

By noting, k_m the stiffness of the analysed sample, we get $k_m = F_r/d$. As $k_m = E'S/h$ where S is the area of sample section and h its height, we deduced the storage modulus E'. The loss modulus is then given by the relationship: $E'' = E' \tan \delta$.

Appendix B

The behaviour of the experimental system studied in this paper can be described by an autonomous single degree-of-freedom conveyor-belt system shown in Fig. A3.

In this model, a mechanical oscillator of unit mass is subjected to a dimensionless friction force $\mu(V)\text{sign}(V)$ where $\mu(V)$ is the velocity dependent friction coefficient and sign the signum function. A modal damping coefficient 2ζ is introduced to take into account dissipation mechanisms other than friction.

In order to determine the sliding velocity range leading to squealing noise, it is necessary to consider the stability of the static equilibrium.

Let us consider the equation of motion in the dimensionless form,

$$\ddot{x} + 2\zeta\dot{x} + x = \mu(V - \dot{x})\text{sign}(V - \dot{x}) \tag{B.1}$$
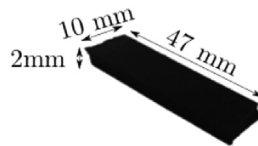

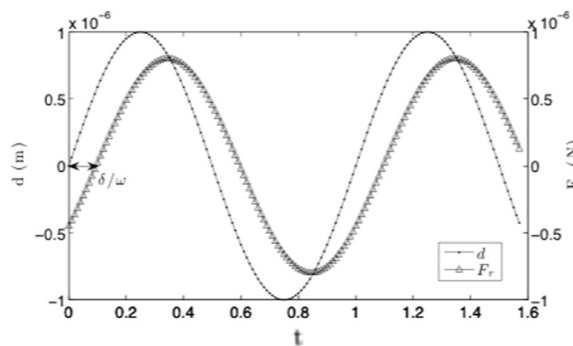**Fig. A1.** Rubber sample used for the DMA measurements.

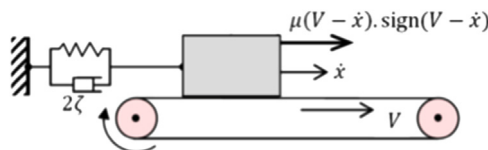**Fig. A2.** Shift phase between the temporal evolution of the imposed displacement and the resulting force.

Fig. A3. The conveyor–belt model.

which applies whenever the relative velocity $v = V - \dot{x}$ is non-zero. In the state space $q = x, q = \dot{x}$, the corresponding set of first-order differential equations is

$$\dot{q} = p$$
$$\dot{p} = -q - 2\zeta p + \mu(V - p)\text{sign}(V - p) \tag{B.2}$$

This set has a unique equilibrium state q_e, p_e found by setting $\dot{q} = \dot{p} = 0$

$$q_e = \mu(V), \quad p_e = 0 \tag{B.3}$$

To determine the local stability of this equilibrium, we superimpose a small disturbance $q = \mu(V) + y$ and $p = z$. After linearization, one obtains in the vicinity of the equilibrium

$$\begin{bmatrix} \dot{y} \\ \dot{z} \end{bmatrix} = \begin{bmatrix} 0 & 1 \\ -1 & -2\zeta - \frac{d\mu}{dv}(V) \end{bmatrix} \begin{bmatrix} y \\ z \end{bmatrix} \tag{B.4}$$

The eigenvalues of the Jacobian matrix provides the required information. They are

$$\lambda_{1,2} = -T \pm \sqrt{T^2 - 1} \quad \text{with } T = \zeta + \frac{1}{2}\frac{d\mu}{dv}(V) \tag{B.5}$$

The nature of the motion about equilibrium is determined by these eigenvalues. The equilibrium is an unstable node when $T \leq -1$, an unstable focus when $-1 < T < 0$, a centre when $T = 0$, a stable focus when $0 < T < 1$, and a stable node when $T \geq 1$. The system undergoes a Hopf bifurcation when $T = 0$, i.e. when the slope of the steady-state friction coefficient becomes less than -2ζ.

Finally, the sliding velocity range for which the system exhibits vibration is such that $d\mu/dv(V) < -2\zeta$. In practice, it is sufficient to measure the steady-state kinetic friction coefficient versus sliding velocity and to apply a fit to accurately determine the first derivative with respect to the relative velocity.

References

[1] J. Oden, J. Martins, Model and computational methods for dynamic friction phenomena, *Computer Methods in Applied Mechanics and Engineering* 52 (1985) 527–634.
[2] K. Popp, P. Stelter, Stick-slip vibrations and chaos, *Philosophical Transactions of the Royal Society of London A: Mathematical, Physical and Engineering Sciences* 332 (1990) 89–105.
[3] N.M. Kinkaid, O.M. O'Reilly, P. Papadopoulos, Automotive disc brake squeal, *Journal of Sound and Vibration* 267 (October) (2003) 105–166.
[4] O. Huajiang, N. Wayne, Y. Yuan, F. Chen, Numerical analysis of automotive disc brake squeal: *a review, International Journal of Vehicle Noise and Vibration* 1 (2005) 25.
[5] O. Giannini, A. Akay, F. Massi, Experimental analysis of brake squeal noise on a laboratory brake setup, *Journal of Sound and Vibration* 292 (April) (2006) 1–20.
[6] N. Coudeyras, S. Nacivet, J.J. Sinou, Periodic and quasi-periodic solutions for multi-instabilities involved in brake squeal, *Journal of Sound and Vibration* 328 (2009) 520–540.
[7] S. Oberst, J.C.S. Lai, Chaos in brake squeal noise, *Journal of Sound and Vibration* 330 (2011) 955–975.
[8] B. Hervé, J.-J. Sinou, H. Mahé, L. Jézéquel, Analysis of squeal noise and mode coupling instabilities including damping and gyroscopic effects, *European Journal of Mechanics* 27 (2008) 141–160.
[9] F.G. De Beer, M.H.a. Janssens, P.P. Kooijman, Squeal noise of rail-bound vehicles influenced by lateral contact position, *Journal of Sound and Vibration* 267 (October) (2003) 497–507.
[10] N. Vincent, J.R. Koch, H. Chollet, J.Y. Guerder, Curve squeal of urban rolling stock-part 1: *state of the art and field measurements, Journal of Sound and Vibration* 293 (June) (2006) 691–700.
[11] Ch. Glocker, E. Cataldi-Spinola, R.I. Leine, Curve squealing of trains: *measurement, modelling and simulation, Journal of Sound and Vibration* 324 (July) (2009) 365–386.
[12] D. Vola, M. Raous, J.A.C. Martins, Friction and instability of steady sliding: *squeal of a rubber/glass contact, International Journal for Numerical Methods in Engineering* 1720 (1999) 1699–1720.
[13] S. Goto, H. Takahashi, T. Oya, Clarification of the mechanism of wiper blade rubber squeal noise generation, *Japan Society of Automotive Engineers* 22 (2001) 57–62.
[14] A. Koenen, A. Sanon, Tribological and vibroacoustic behavior of a contact between rubber and glass (application to wiper blade), *Tribology International* 40 (October) (2007) 1484–1491.
[15] G. Bódai, T.J. Goda, Friction force measurement at windscreen wiper/glass contact, *Tribology Letters* 45 (January) (2012) 515–523.
[16] J. Le Rouzic, A. Le Bot, J. Perret-Liaudet, M. Guibert, A. Rusanov, L. Douminge, F. Bretagnol, D. Mazuyer, Friction-induced vibration by Stribeck's law: *application to wiper blade squeal noise, Tribology Letters* 49 (January) (2013) 563–572.
[17] G. Sheng, J.H. Lee, V. Narravula, D. Song, Experimental characterization and analysis of wet belt friction and the vibro-acoustic behavior, *Tribology International* 44 (March) (2011) 258–265.
[18] Y.J. Luo, Z.Y. Gao, Estimation of friction coefficient related to squeal in cutting, *Advanced Materials Research* 314–316 (2011) 603–608.
[19] A.I. Krauter, Generation of squeal/chatter in water-lubricated elastomeric bearings, *Journal of Tribology* 103 (1981) 406–412.
[20] F. Kavarana, B. Rediers, Squeak and rattle—state of the art and beyond, *Sound and Vibration* 35 (2001) 56–64.
[21] J. Woodhouse, S.K. Wang, The frequency response of dynamic friction: *model comparisons, Journal of the Mechanics and Physics of Solids* 59 (November) (2011) 2294–2306.
[22] T. Butlin, J. Woodhouse, A systematic experimental study of squeal initiation, *Journal of Sound and Vibration* 330 (October) (2011) 5077–5095.
[23] A. Elmaian, F. Gautier, C. Pezerat, J.-M. Duffal, How can automotive friction-induced noises be related to physical mechanisms? *Applied Acoustics* 76 (February) (2014) 391–401.
[24] A. Akay, Acoustics of friction, *The Journal of the Acoustical Society of America* 111 (2002) 1525.
[25] R.A. Ibrahim, Friction-induced vibration chatter squeal and chaos. part II: *dynamics and modelling, ASME Journal of Applied Mechanics* 47 (1994) 227–253.

[26] R.A. Ibrahim, Friction-induced vibration chatter squeal and chaos. part I: *mechanics of contact and friction, ASME Journal of Applied Mechanics* 47 (1994) 208–226.
[27] T. Butlin, J. Woodhouse, Friction-induced vibration: *should low-order models be believed? Journal of Sound and Vibration* 328 (November) (2009) 92–108.
[28] N. Hoffmann, M. Fischer, R. Allgaier, L. Gaul, A minimal model for studying properties of the mode-coupling type instability in friction induced oscillations, *Mechanics Research Communications* 29 (July) (2002) 197–205.
[29] J. Scheibert, D.K. Dysthe, Role of friction-induced torque in stick-slip motion, *Europhysics Letters* 92 (December (54001)) (2010) 1–6.
[30] R.I. Leine, D.H. Van Campen, A. De Kraker, Stick-slip vibrations induced by alternate friction models, *Nonlinear Dynamics* 16 (1998) 41–54.
[31] E. Berger, Friction modeling for dynamic system simulation, *Applied Mechanics Reviews* 55 (2002) 535.
[32] J. Awrejcewicz, P. Olejnik, Analysis of dynamic systems with various friction laws, *Applied Mechanics Reviews* 58 (2005) 389.
[33] P. Dupont, B. Armonstrong, Hayward V. Elasto-plastic friction model: contact compliance and stiction. Proceedings of the American Control Conference, pages 1073–1077, 2000.
[34] V. Lampaert, F. Al-Bender, J. Swevers. A generalized Maxwell-slip friction model appropriate for control purposes. *International Conference Physics and Control*, vol. 4, 2003, pp. 1170–1177.
[35] J.H. Dieterich, Time-dependent friction and the mechanics of stick-slip, *Pure and Applied Geophysics* 116 (1978) 790–806.
[36] J.H. Dieterich, Modeling of rock friction—1. Experimental results and constitutive equations, *Journal of Geophysical Research: Solid Earth* 84 (1979) 2161–2168.
[37] A. Ruina, Slip instability and state variable friction laws, *Journal of Geophysical Research: Solid Earth* 88 (1983) 10359–10370.
[38] A. Canudas de Wit, H. Olsson, K.J. Aström, P. Lischinsky, A new model for control of systems with friction, *IEEE Transactions on Automatic Control* 40 (1995) 419–425.
[39] C.A. Brockley, P.L. Ko, Quasi-harmonic friction-induced vibration, *Journal of Tribology* 92 (1970) 550–556.
[40] H. Hetzler, D. Schwarzer, W. Seemann, Analytical investigation of steady-state stability and Hopf-bifurcations occurring in sliding friction oscillators with application to low-frequency disc brake noise, *Communications in Nonlinear Science and Numerical Simulation* 12 (February) (2007) 83–99.
[41] A.A. Polycarpou, A. Soom, Measured transitions between sticking and slipping at lubricated line contacts, *Journal of Vibration and Acoustics* 117 (1993) 294–299.
[42] A.A. Polycarpou, A. Soom, Application of a two-dimensional model of continuous sliding friction to stick-slip, *Wear* 181–183 (February) (1995) 32–41.
[43] F. Wu-Bavouzet, J. Clain-Burckbuchler, A. Buguin, P.-G. De Gennes, F. Brochard-Wyart, Stick-slip: *wet versus dry*, *The Journal of Adhesion* 83 (September) (2007) 761–784.
[44] F. Deleau, D. Mazuyer, A. Koenen, Sliding friction at elastomer/glass contact: *influence of the wetting conditions and instability analysis, Tribology International* 42 (January) (2009) 149–159.
[45] M.C. Audry, C. Fretigny, A. Chateauminois, J. Teissere, E. Barthel, Slip dynamics at a patterned rubber/glass interface during stick-slip motions, *The European Physical Journal. E, Soft Matter* 35 (September (83)) (2012).
[46] I.A. Lyashenko, A.V. Khomenko, A.M. Zaskoka, K.S. Zhmaka. Hysteresis phenomena in the stick-slip motion at the boundary friction mode. *Proceedings of the International Conference Nanomaterials: Applications and Properties*, Vol. 2, 2013, pp. 2–5.
[47] M. Woydt, R. Wäsche, The history of the Stribeck curve and ball bearing steels: *the role of Adolf Martens, Wear* 268 (May) (2010) 1542–1546.
[48] M. Denny, Stick-slip motion: *an important example of self-excited oscillation, European Journal of Physics* 25 (March) (2004) 311–322.
[49] K. Nakano, S. Maegawa, Occurrence limit of stick-slip: *dimensionless analysis for fundamental design of robust-stable systems, Lubrication Science* 22 (2010) 1–18.
[50] J.H.H. Bongaerts, K. Fourtouni, J.R. Stokes, Soft-tribology: *lubrication in a compliant PDMS-PDMS contact, Tribology International* 40 (October) (2007) 1531–1542.
[51] J. Le Rouzic, J. Perret Liaudet, A. Carbonelli, A. Le Bot, D. Mazuyer. Some experimental and analytical results on self-excited vibration of a dynamic sliding system in the case of Stribeck law for friction coefficient. *ASME 2011 International Design Engineering Technical Conferences and Computers and Information in Engineering Conference*, Vol. 4, 2011, pp. 207–215.
[52] J. Perret Liaudet, F. Dalzin, A. Le Bot, D. Mazuyer. Some results about squealing of a lubricated sliding contact with the Stribeck effect. *SIA International Conference on Light-weighting and Acoustical Materials in Vehicles*, Vol. R-2013-07-07, 2013, p. 5.